Dipolar Cairo lattice: Geometrical frustration and short-range correlations

Michael Saccone, Kevin Hofhuis, Yen-Lin Huang, Scott Dhuey, Zuhuang Chen, Andreas Scholl, Rajesh V. Chopdekar, Sebastiaan van Dijken, and Alan Farhan

The dipolar Cairo lattice: geometrical frustration and short-range correlations

Michael Saccone,[1] Kevin Hofhuis,[2, 3] Yen-Lin Huang,[4] Scott Dhuey,[5] Zuhuang Chen,[6]
Andreas Scholl,[7] Rajesh V. Chopdekar,[7] Sebastiaan van Dijken,[8] and Alan Farhan[3, 7, 8, ∗]

[1]*Physics Department, University of California, 1156 High Street, Santa Cruz, CA 95064, USA*
[2]*Laboratory for Mesoscopic Systems, Department of Materials, ETH Zurich, 8093 Zurich, Switzerland*
[3]*Laboratory for Multiscale Materials Experiments,*
Paul Scherrer Institut, 5232 Villigen PSI, Switzerland
[4]*Department of Materials Science and Engineering,*
University of California, Berkeley, California 94720, USA
[5]*Molecular Foundry, Lawrence Berkeley National Laboratory (LBNL), 1 Cyclotron Road, Berkeley, CA 94720, USA*
[6]*School of Materials Science and Engineering, Harbin Institute of Technology, Shenzhen, Guangdong 518055, China*
[7]*Advanced Light Source, Lawrence Berkeley National Laboratory (LBNL), 1 Cyclotron Road, Berkeley, CA 94720, USA*
[8]*NanoSpin, Department of Applied Physics, Aalto University School of Science, P.O. Box 15100, FI-00076 Aalto, Finland*
(Dated: September 24, 2019)

We have studied low-energy configurations in two-dimensional arrays consisting of Ising-type dipolar coupled nanomagnets lithographically defined onto a two-dimensional Cairo lattice, thus dubbed the dipolar Cairo lattice. Employing synchrotron-based photoemission electron microscopy (PEEM), we perform real-space imaging of moment configurations achieved after thermal annealing. These states are then characterized in terms of vertex populations, spin- and emergent magnetic charge correlations, and a topology-enforced emergent ice rule. The results reveal a strong dominance of short-range correlations and the absence of long-range order, reflecting the high degree of geometrical spin frustration present in this example of an artificial frustrated spin system.

I. INTRODUCTION

Artificial spin ice systems [1–16], initially introduced as two-dimensional analogues to pyrochlore spin ice [17], enabled the direct visualization of the consequences of geometrical frustration using appropriate magnetic imaging techniques. In particular, the introduction of artificial spin ices that exhibit thermally induced moment fluctuations paved the way to explore the statistical physics of geometrical frustration [3–6], emergent magnetic monopoles and macroscopic spin ice degeneracy [18, 19], in addition to first attempts in achieving artificial spin glasses [20]. Furthermore, this newly acquired possibility lead to a whole new line of research, where novel two-dimensional lattices comprising Ising-type nanomagnets are being designed, that would exhibit exotic emergent phenomena that go beyond spin ice physics. Prominent examples are the observation of emergent magnetic charge screening and polaronic states in systems with mixed coordination numbers [21–23], field-induced phase coexistence in a quadrupole lattice [24], in addition to systems exhibiting topological frustration [25–28] and the ability to directly control the degree of spin frustration at the nanoscale [29, 30]. All these artificial frustrated systems have also shown promise in potential applications in the field of spintronics and magnonics [31–35]. With regard to systems with mixed coordination numbers, the systems investigated, so far [21–23], while exhibiting high degeneracy levels, have been shown to exhibit long-range charge-ordered states at lower temperatures. This raises the question whether another system with mixed coordination numbers can be proposed, which exhibits a high degree of spin frustration and remains in a state that is dominated by short-range spin correlations, thus adding an additional system to the family of artificial frustrated systems [36].

In this paper we address this question, by exploring geometrical frustration achieved in a two-dimensional artificial spin system, where Ising-type nanomagnets are placed onto the sites of a so-called Cairo lattice (see Fig. 1). The Cairo lattice geometry has risen to prominence as an alternative approach in achieving geometrical spin frustration leading to a variety of new properties and ground state configurations [37–40].

The manuscript is organized as follows: in the methods section, we describe the process of sample fabrication and the magnetic imaging technique. Micromagnetic simulations of relevant coupling strengths are also described. This is followed by a report on thermal annealing and magnetic imaging experiments including a quantitative analysis of all observations. The data obtained are discussed in terms of short-range spin correlations, highlighting the high degree of geometrical spin- and vertex frustration achieved in this artificial spin system, together with the observation of polaronic states. We conclude with a summary and outlook on potential future investigations featuring the dipolar Cairo lattice.

II. METHODS

We used electron beam lithography to fabricate dipolar Cairo lattices. Following e-beam exposure and development of a 70-nm-thick polymethylmethacrylate (PMMA)
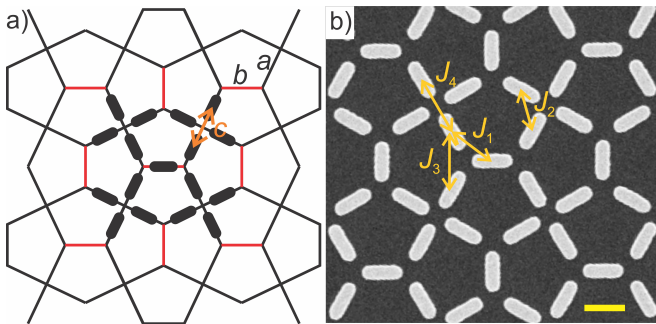
∗ alan.farhan@gmx.net

FIG. 1. (a) Dipolar Cairo lattice. Dipolar-coupled Ising-type nanomagnets (stadium-shaped islands) occupy the sites of the pentagonal Cairo lattice (lines the background). Lattice parameters $a = 472$ nm and $b = 344$ nm are kept constant, while the lattice parameter $c = 376$ nm, 450 nm, 500 nm and 600 nm is varied, to tune the coupling strengths between the nanomagnets. (b) Scanning electron microscopy (SEM) image of one of the dipolar Cairo lattices consisting of nanomagnets with lengths and widths of 300 nm and 100 nm, respectively. The lattice parameter c is varied, so that the balance between the coupling strengths J_1, J_2, J_3 and J_4 can be tuned at the nanoscale. The yellow scale bar indicates a length of 300 nm.

resist layer on a silicon (100) substrate, a 2.6 nm thick Permalloy ($Ni_{80}Fe_{20}$) thin film was deposited (base pressure: 2×10^{-7} Torr), along with a 2 nm thick aluminum capping layer to avoid fast oxidation of the sample. Next, a lift off process in acetone removed all unwanted magnetic material. The resulting patterned nanomagnets have a length of 300 nm and a width of 100 nm and they are arranged onto a Cairo lattice with lattice parameters $a = 472$ nm and $b = 344$ nm (see Fig. 1a). The coupling strengths J_i (see Fig. 1b) are directly tuned by varying the lattice parameter c (see Fig. 1a), which is given values of 376 nm, 450 nm, 500 nm and 600 nm. Each array covered an area of 60×60 μm^2.

Magnetic imaging was performed by synchrotron-based photoemission electron microscopy (PEEM) [41], employing x-ray magnetic circular dichroism (XMCD) at the Fe L_3 edge [42]. XMCD images were obtained by pixelwise division of images recorded with circular right and left polarized light. The resulting dark and bright contrast provides a direct measure of the orientation of the local magnetization. Magnetic moments pointing towards the incoming X-rays appear dark and moments opposing the X-ray direction appear bright. If a magnetic moment is oriented 90° with respect to the X-ray direction, it does not show contrast and appears grey. Because the nanomagnets of the dipolar Cairo lattice are patterned along different directions, deterministic imaging of all magnetic moments is challenging (see Fig. 1b). To ensure that all magnetic moments have a non-zero projection onto the incoming X-rays, we rotated the sample by 15°.

We performed micromagnetic simulations using Mu-Max3 [44] to determine the coupling energies in the dipolar Cairo geometry. In the simulations, nanomag-

nets with a size of $300 \times 100 \times 3$ nm^3 were discretized into $1.95 \times 1.95 \times 3$ nm^3 cells. Typical material parameters for Permalloy were used: $M_s = 790$ kA/m, $A = 13 \times 10^{-12}$ J/m. The magnetic anisotropy was set to zero. As the Gilbert damping parameter we used $\alpha = 1.0$ to allow the simulations to relax quickly. The coupling energies were derived from simulating different nearest-neighbour nanomagnet pairs. To do this, we first determined the low and high energy states E_1 and E_2, which are given by $E_1 = 2E_{nanomagnet} - E_{coupling}$ and $E_2 = 2E_{nanomagnet} + E_{coupling}$. Here, only the coupling energy $E_{coupling}$ depends on the orientation and distance between the nanomagnets. The coupling energy is then given by $E_{coupling} = (E_2 - E_1)/2$. The simulations were performed for a lattice parameter c varying from 350 nm to 600 nm in 12.5 nm steps. The same approach was applied in calculating vertex type energies as a function of lattice parameter c.

III. RESULTS

A. Energy landscape and micromagnetic simulations of coupling strengths

Before we summarize the experimental observations, it is important to understand and characterize the dipolar Cairo lattice energetically. As in other artificial spin ice systems [1, 21, 22, 29, 30], the magnetic configurations can be categorized into vertex types (see Fig. 2). The dipolar Cairo lattice exhibits four- and three-nanomagnet vertices similar to those observed in the square- and Kagome spin ice geometry, respectively [1, 4]. The four-nanomagnet vertex types are listed with increasing dipolar energy in Fig. 2a, going from Type I to Type IV. Type I and Type II obey the so-called ice rules, which dictate two moments to point into the vertex and two moments to point out of the vertex (see Fig. 2a). In an emergent magnetic charge picture [18, 19, 45, 46], these vertices exhibit a zero magnetic charge at the vertex of $Q = 0$. Type III vertices break the ice rule, as three moments point into the vertex and one out or vice versa. In the magnetic charge representation, they can be seen as topological defects bearing a non-zero effective magnetic charge residing at the vertex ($Q = \pm 2q$). Type IV vertices (($Q = \pm 4q$) represent the highest energy states and are energetically so unfavorable that they are not observed in our experiments. The three-nanomagnet vertices can be compared to the known Kagome vertices [4, 10, 47], however, with one crucial difference: Because $a \neq b$ and the varying lattice parameter c, the distances between nanomagnets at the three-nanomagnet vertices can be non-equal, resulting in different coupling strengths ($J_1 \geq J_3$). Therefore, the six-fold degenerate ice-rule (two-moments-in-one-moment-out or vice versa) configurations are now split into two different vertex types. Moment alignments that minimize the stronger J_1 interactions (coupling between black and red moments in Fig. 2b) are lower in
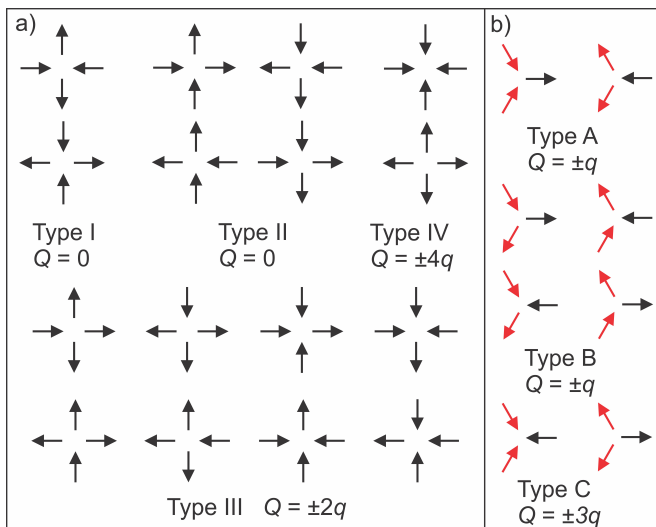
FIG. 2. (a) Vertex types at four-nanomagnet vertices listed with increasing dipolar energy from Type I to Type IV. Type I and Type II are the so-called ice-rule obeying configurations and exhibit a zero net emergent magnetic charge at the vertex ($Q = 0$). Type III vertices break the ice rules and can be described as vertex defects that possess an non-zero net magnetic charge at the vertex ($Q = \pm2q$). Type IV vertices have the highest energy and are never observed in our experiments. (b) Vertex types at three-nanomagnet vertices categorized with increasing dipolar energy from Type A to Type C. Red arrows mark those moments that are coupled with each other via J_3, while the red and black arrows are coupled via J_1.

FIG. 3. Evolution of all relevant coupling strengths J_1 (blue dots and curve), J_2 (red dots and curve), J_3 (yellow dots and curve) and J_4 (purple dots and curve) plotted as a function of lattice parameter c.

B. Thermal annealing and XMCD imaging

Now that the dipolar Cairo lattice has been introduced, we turn our attention to thermal annealing experiments. Similar to previous work on artificial frustrated systems [4, 5, 19, 22, 29], the prepared structures were kept at room temperature and in vacuum for several days. Then, the samples were transferred into the PEEM and cooled down 20-30 K below the temperature where thermally-induced moment fluctuations start to occur within the nanomagnets on the time scale of several seconds [19, 22, 29]. Cooling below the so-called blocking temperature ($T_B = 130$ K in our system) ensures that configurations remain frozen during XMCD imaging after thermal annealing. For each lattice parameter ($c = 376$ nm, 450 nm, 500 nm and 600 nm), this annealing procedure is performed five times to provide sufficient statistics. To ensure that observations are not linked to lithographic defects, a different array on the sample was imaged, after each annealing protocol.

Figure 4 shows XMCD images of dipolar Cairo lattices. For all values of the lattice parameter c, long-range ordering is absent by pure visual inspection. A first quantitative characterization of these observations is obtained by plotting the vertex type populations achieved as a function of lattice parameter c (see Fig. 4d and 4e). The four-nanomagnet vertices show a nearly linear decrease in the Type I ground state population, while Type II vertices are rising with increasing lattice parameter c. Type III vertex defects are almost absent up to $c = 450$ nm, but appear in lattices with $c = 500$ nm and $c = 600$ nm. The diminishing energy difference between all four-nanomagnet vertices (see dashed curves in Fig. 4d) is likely what allows these ice rule violations to occur. In contrast to the four-nanomagnet vertices, the pop-

energy and are labeled Type A (see Fig. 2b). Configurations that minimize the weaker interaction J_3, but maximize one of the two J_1 interactions, are higher in energy and are labeled Type B vertices. Configurations breaking the ice-rule remain energetically equivalent and are now branded Type C. The unique feature in the dipolar Cairo lattice is that the balance between the competing interactions J_1 and J_3 can be tuned at the nanoscale from being vastly different to being totally equal. In the latter case, Type A and Type B vertices become energetically equivalent again. In other words, one can turn the spin ice degeneracy at the three-nanomagnet vertices on and off, by varying the lattice parameter c. In Fig. 3 we plot all coupling strengths J_1 to J_4 as a function of c (see Methods). According to these simulation results, J_1 and J_2 as well as J_3 and J_4 equalize around $c = 500$ nm. Equalization of J_1 and J_3 and thus a restoration of the spin ice degeneracy (Type A Energy = Type B Energy) is predicted around lattice parameter $c = 600$ nm (blue and yellow curves in Fig. 3). Mircomagnetic vertex type energy calculations confirm this observation (see Fig. 4d and 4e).
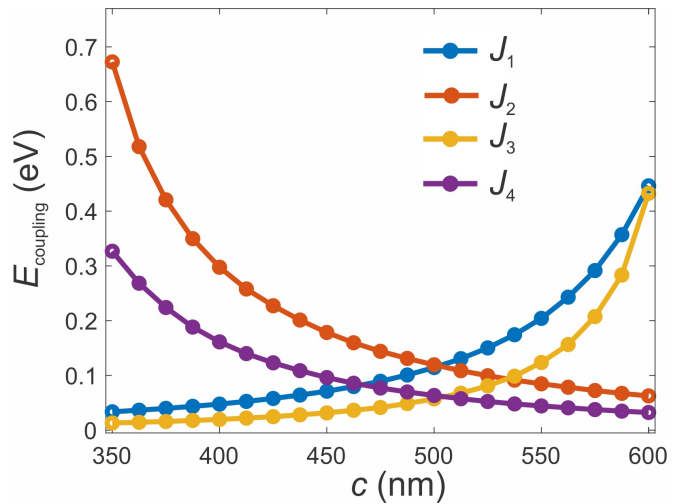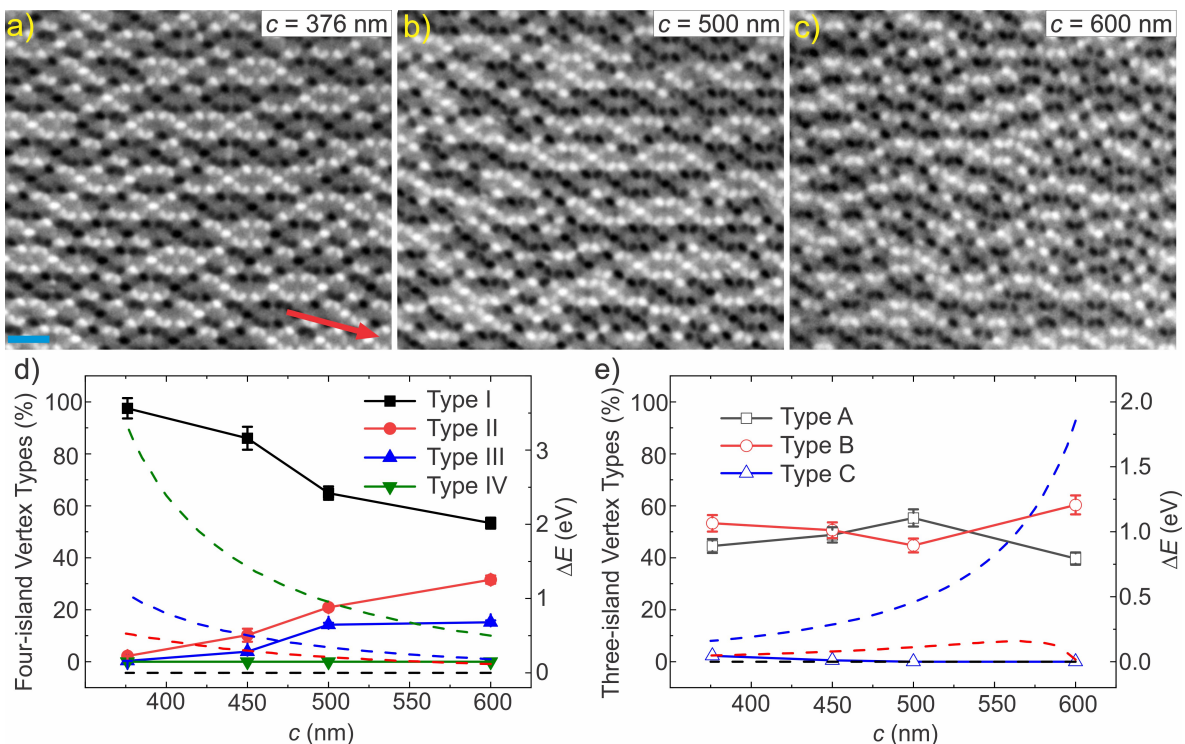
FIG. 4. XMCD images (recorded at $T = 100$ K) of a low-energy moment configuration achieved, following thermal annealing in (a) dipolar Cairo lattice with lattice parameter $c = 376$ nm, (b) $c = 500$ nm and (c) $c = 600$ nm. The incoming X-ray direction is indicated by a large red arrow. The XMCD dark-and-bright contrast gives a direct measure of the magnetization direction relative to the incoming X-ray propagation vector. Magnetic moments pointing towards the incoming X-rays appear dark, while moments opposing the X-ray direction appear bright. The blue bar indicates a length of 1 μm. (d) Vertex type populations at four-nanomagnet vertices plotted as a function of lattice parameter c. (e) Three-nanomagnet vertex-type population under the variation of c. The error bars in (d) and (e) represent standard deviations of the mean resulting from XMCD measurements performed after each of the five repeated annealing cycles. The dashed curves in (d) and (e) represent the corresponding relative vertex type energies (from micromagnetic simulations) plotted as a function of c.

ulations of three-nanomagnet vertex Types do not depend much on c (see Fig. 4e). Intuitively, one would expect, that full dominance by ground state Type I vertices would lead to the ergodicity of Type A and Type B three-nanomagnet vertices, comprising $1/3$ and $2/3$ of the population, respectively. However, the number of Type A and Type B vertices is approximately equal, implying that another mechanism is at play. Curiously, only the 600 nm system moves towards ergodicity as the Type A and B vertices equalize in energy (see dashed curves in Fig. 4e) and ice rule obedience at the four-nanomagnet vertices diminishes. In summary, the dipolar Cairo lattice aims to establish a Type I ground state configuration at the four-nanomagnet vertex sites, while the three-nanomagnet vertices strictly obey the ice rule (almost no Type C vertices). However, the proportion of Type A vertices remains higher than expected.

C. Emergent ice-rule and polaronic states

The Cairo lattice is topologically equivalent to the recently investigated Shakti lattice [21, 48], implying that the same mode of toplogical frustration prevents long-range order in the system. Looking at magnetic moment configurations (see arrows in Fig. 5a and 5b) and magnetic charge patterns (blue and red circles in Fig. 5a and 5b), long-range order seems absent. In analogy to the Shakti lattice, the Cairo lattice largely obeys an emergent ice-rule. This rule dictates that a system with this geometry and only Type A, Type B, and Type I vertices must distribute Type A and Type B vertices (filled and empty circles in Fig. 5a, 5b and 5c, respectively) equally within a four-vertex plaquette (see Fig. 5c). The emergent ice rule explains the discrepancy from ergodic Type A and Type B vertex populations by bringing them closer to 50% (see Fig. 4e). Strict emergent ice-rule obedience is particularly striking in the case of strong nearest-neighbor coupling at the four-nanomagnet vertices ($c = 376$ nm) due to the lack of Type II-IV vertices, providing a direct explanation why the Cairo lattice lacks features of long-range order. As the lattice parameter c is increased, we see an increasing number of violations to this emergent ice-rule (see Fig. 5b), which is linked to a rise in Type B vertex population with c (see Fig. 4e). Interestingly, this is also coupled to an increase in Type III
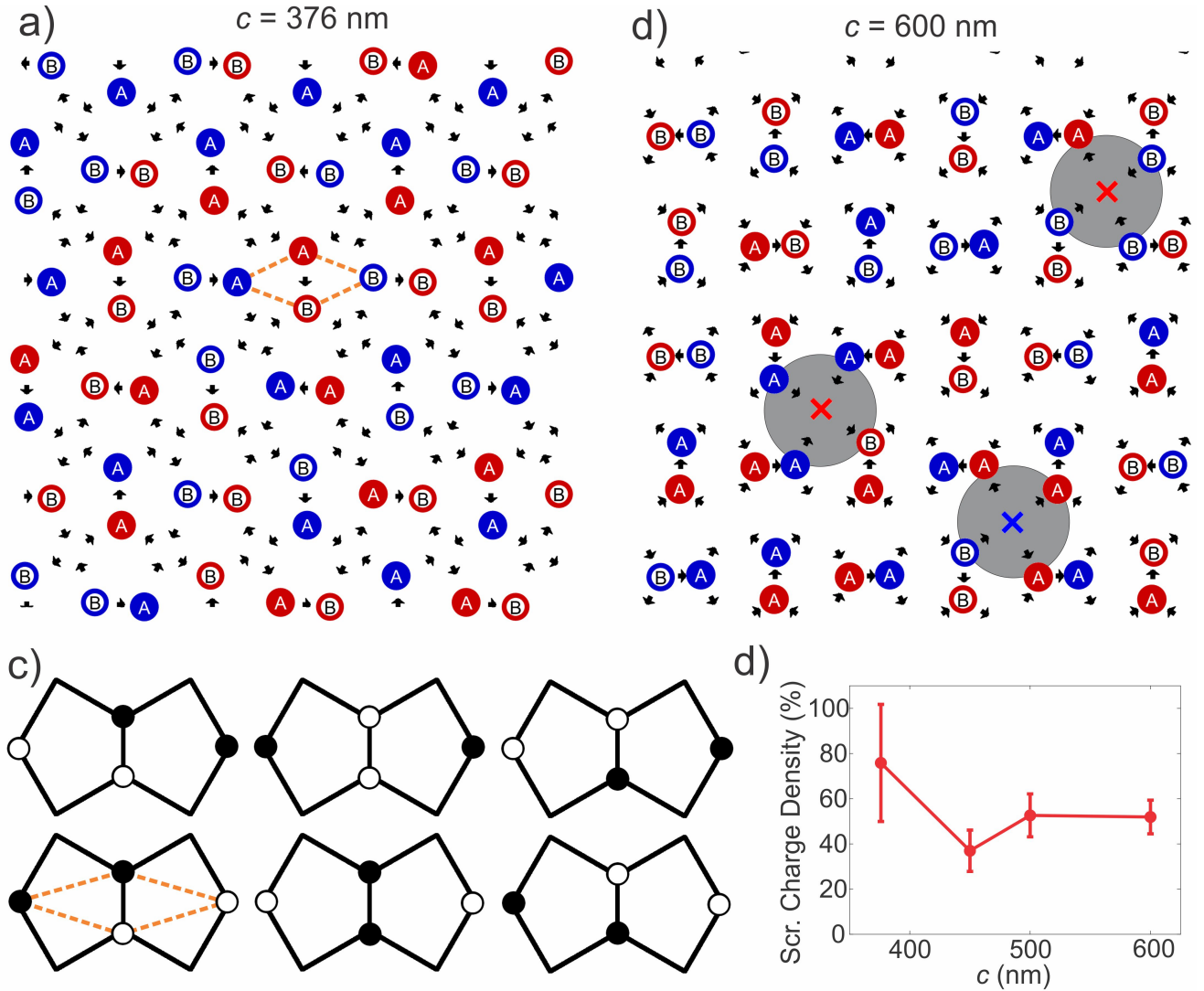
FIG. 5. (a),(b) Magnetic moment and charge configurations achieved after thermal annealing for Cairo lattices with (a) $c = 376$ nm and (b) $c = 600$ nm. Positive $+q$ and negative $-q$ charges are depicted in with red and blue circles at three-nanomagnet vertices, respectively. Filled circles represent Type A vertices, while Type B vertices are shown with empty circles. Type III charge defects $\pm 2q$ are represented with red (+) and blue (-) crosses. Grey circles in (b) highlight screened charge defects. (c) Four-vertex plaquettes obeying the emergent ice-rule. Six variations of the two Type A (filled circles) and two Type B (empty circles) vertices within each plaquette obey this emergent ice-rule. Dashed orange kites in (a) and (c) highlight one of the plaquettes. (d) Percentage of screened Type III charge defects plotted as a function of lattice parameter c. The error bars represent standard deviations resulting from observations after five annealing cycles.

vertex defects at the four-nanomagnet vertex sites (blue and red crosses in Fig. 5b). These vertex defects can be seen as emergent magnetic charge defects ($Q_{z4} = \pm 2q$), with a major part of them getting screened by surrounding magnetic charges ($Q_{z3} = \pm q$), which reside at neighboring three-nanomagnet vertices (see Fig. 5b). In other words, the sum of magnetic charges residing at four- and three-nanomagnet vertices is zero ($\sum Q_{z4} + Q_{z3} = 0$). The fraction of Type III charge defects that are perfectly screened is plotted in Fig. 5d. A random distribution of Q_{z3} charges would only screen four out of sixteen possible states, but the screened fraction remains significantly higher than 25% for all values of c. The outlying point at

$c = 376$ nm is likely a result of the low number of Type III vertices (9 out of 1600 possible four-nanomagnet vertices) at this lattice parameter. Polaronic states are a typical feature for artificial spin ices with mixed coordination numbers as predicted and observed in the dipolar dice- and pentagonal lattice [22, 23]. However, in contrast to these cases, which feature long-range charge-ordered ground states, the dipolar Cairo lattice does not seem to show any tendency towards long-range ordering, whether defined by magnetic charges or magnetic moments.
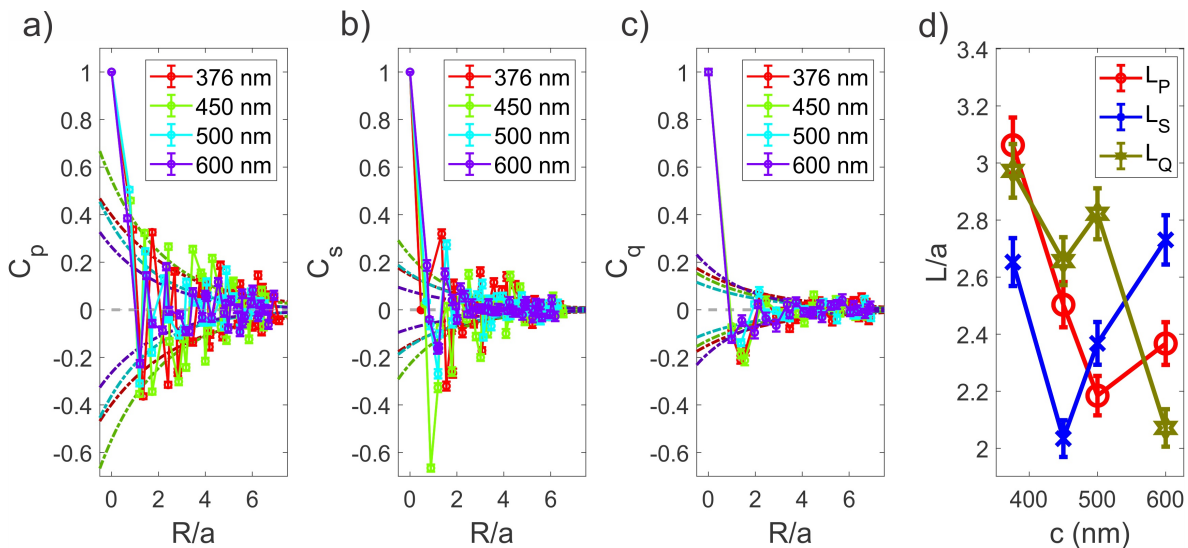
FIG. 6. Correlation functions and extracted correlation lengths of all annealed ground states. All length scales are stated in proportion to the lattice parameter $a = 472$ nm. (a),(b) Spin-spin correlations between the "p" subset of spins (a) and the "s" subset of spins (b). (c) Charge-charge correlation function of all charges in the lattice. All correlation function seem to be exponentially encapsulated as a function of distance. (d) Correlation lengths as a function of lattice parameter c. The error bars represent standard deviations resulting from XMCD measurements performed after each of the five repeated annealing cycles.

D. Correlations and short-range ordering

The existence of preferred vertex types and emergent ice-rule obedience suggests quantifiable short-range ordering within the system. Additionally, the emergent magnetic charges may possess some hidden order [49], providing another structure to the system not immediately apparent in the magnetic orientation of the nanomagnets. Here we extract the spin-spin and charge-charge correlation functions, fit these functions to an exponential, and from those fits compute the spin and charge correlation lengths.

The geometry of the Cairo lattice creates two subsets of spins, those only partaking in three-nanomagnet vertices and those in both three and four-nanomagnet vertices. The former we label "p" spins because they are parallel and perpendicular to each other and the latter we label "s" spins as they are skewed from one another. The two subsets experience different types of interactions and therefore should not be assumed to have correlation functions that behave the same. The correlation functions themselves are calculated in a manner typical of Ising type systems:

$$C(\mathbf{r}_{ij}) = S_i S_j \qquad (1)$$

where $S_i = \pm 1$ to represent the Ising state of spin i and r_{ij} is the distance between spins i and j. There is normally a thermal average, but it is omitted here as the analysis is performed on single configurations. The correlation functions are made a function of distance, r, by

averaging over C_{ij} where $r - \Delta/2 < r_{ij} < r + \Delta/2$:

$$[C(r)]_{av} = \frac{1}{N_{pair}} \sum_{ij}' C(\mathbf{r}_{ij}). \qquad (2)$$

Here, N_{pair} is the number of pairs of ij over which the sum is taken. A charge correlation function is defined similarly as

$$C_{Q,ij} = \Theta(Q_i Q_j), \qquad (3)$$

where Q_i is the magnetic charge at a vertex labelled i and $\Theta(x)$ returns the sign of the argument or zero if the argument is zero. Again, the function is averaged over similar distances to create $C(r)$. The magnitude of this parameter and the spin correlations are fitted to an exponential decay function, $|C(r)| = A \exp(-r/L)$, where A is merely a fitting constant and L is the correlation length (see dashed curves in Fig. 6a-c). Three categories of lengths are extracted for the p spins, s spins, and charges (L_p, L_s, and L_Q respectively). The correlation lengths are plotted as a function of c in Fig. 6d.

All correlation functions (Fig. 6a-c) are fit to exponentials with confidence intervals of 95%. They typically oscillate between positive and negative values as antiferromagnetic spin ordering and alternating charge ordering are preferred. The higher value of the spin correlation functions (Fig. 6a-b) compared to the charge-charge correlation function (Fig. 6c) indicates a dominant preference for spin ordering over charge ordering. Though they are less likely to correlate, the lengths over which charges correlate are similar to the spin correlation

lengths (Fig. 6d). In accord with the geometrical frustration picture, the spin-spin correlation lengths are all on the order of 2-3 lattice parameters a, approximately the size of a single four-vertex plaquette (see Fig. 5c). Long-range order is clearly absent. Despite the absence of a clear trend, the "p" and "q" lengths roughly decrease with increasing c and the "s" length fluctuates up and down with c. Each of the three correlation lengths are dominant for at least one value of c. These non-monotonic behaviors further highlight the flexibility in defining ordering preferences in the dipolar Cairo lattice.

IV. SUMMARY AND OUTLOOK

The Cairo lattice presents rich, tunable frustration. Its geometry allows for lattice parameter c to influence 4 magnetic coupling constants (Fig. 3). All annealed systems with c varying from 376 nm to 600 nm contained no apparent long-range order (Fig. 4), as verified by correlation function and correlation length calculations (Fig. 6). An emergent ice-rule (Fig. 5a-c) explains the high degree of frustration and the oddity of similar concentrations of Type A and Type B vertices (Fig. 4) and the lack of long-range order. In contrast to the Shakti lattice where this rule was first observed [21], long-range charge ordering is absent (Fig. 5a-b and Fig. 6d). Reducing the four-nanomagnet vertex coupling by increasing c leads to an increase in Type III charge defects ($Q_{z4} = \pm 2q$), which have a tendency to be screened by surrounding charges $Q_{z3} = \pm q$, that reside at three-nanomagnet vertices.

However, an important open question remains, namely that of the true ground state of this system and the role of long-range dipolar interactions that go beyond J_1 to J_4 (see Fig. 1b). This question might be addressed through computational studies [46] or improvements in the annealing procedure. Furthermore, it will be interesting to study the thermal stability of polaronic states with temperature dependent experiments [19, 22]. The degree to which these charges are screened and their mobility may provide ideal conditions for new DebyeHckel plasmas [19]. Such dynamic XMCD measurements might also shed light on the potential observation of emergent reduced dimensionality [50], a scenario that cannot be fully excluded with absolute certainty, based on the current results. Furthermore, relaxation time scale variations, as a result of vertex frustration [51] might also provide insight into the ground state question.

V. ACKNOWLEDGEMENTS

[1] R. F. Wang, C. Nisoli, R. S. Freitas, J. Li, W. McConville, B. J. Cooley, M. S. Lund, N. Samarth, C. Leighton, V. H. Crespi, and P. Schiffer, Nature **439**, 303 (2006).

[2] S. Ladak, D. E. Read, G. K. Perkins, L. F. Cohen, and W. R. Branford, Nature Physics **6**, 359 (2010).

[3] J. P. Morgan, A. Stein, S. Langridge, and C. H. Marrows, Nature Physics **7**, 75 (2011).

[4] A. Farhan, P. M. Derlet, A. Kleibert, A. Balan, R. V. Chopdekar, M. Wyss, L. Anghinolfi, F. Nolting, and L. J. Heyderman, Nature Physics **9**, 375 (2013).

[5] A. Farhan, P. M. Derlet, A. Kleibert, A. Balan, R. V. Chopdekar, M. Wyss, J. Perron, A. Scholl, F. Nolting, and L. J. Heyderman, Physical Review Letters **111**, 057204 (2013).

[6] J.M. Porro, A. Bedoya-Pinto, A. Berger, and P. Vavassori, New Journal of Physics **15**, 055012 (2013).

[7] N. Rougemaille, F. Montaigne, B. Canals, A. Duluard, D. Lacour, M. Hehn, R. Belkhou, O. Fruchart, S. El Moussaoui, A. Bendounan, and F. Maccherozzi, Physical Review Letters **106**, 057209 (2011).

[8] L. A. S. Mól, A. R. Pereira, and W. A. Moura-Melo, Physical Review B **85**, 184410 (2012).

[9] I. S. Shishkin, A. A. Mistonov, I. S. Dubitskiy, N. A. Grigoryeva, D. Menzel, and S. V. Grigoriev, Physical Review B **94** 064424 (2016).

[10] A. Farhan, P. M. Derlet, L. Anghinolfi, A. Kleibert, and L. J. Heyderman, Physical Review B **96**, 064409 (2017).

[11] E. Östman, H. Stopfel, I.-A. Chioar, U. B. Arnalds, A. Stein, V. Kapaklis, and Björgvin Hjörvarsson, Nature Physics **14**, 375 (2018).

[12] Y. Shevchenko, A. Makarov, K. Nefedev, Physics Letters A **381**, 428 (2017).

[13] R. P. Loreto, F. S. Nascimento, R. S. Gonçalves, J. Borme, J. C. Cezar, C. Nisoli, A. R. Pereira, and C. I. L. de Araujo, Journal of Physics: Condensed Matter **31**, 025301 (2018).

[14] R. Macêdo, G. M. Macauley, F. S. Nascimento, and R. L. Stamps, Physical Review B **98**, 014437 (2018).

[15] S. Gliga, G. Hrkac, C. Donnelly, J. Büchi, A. Kleibert, J. Cui, A. Farhan, E. Kirk, R. V. Chopdekar, Y. Masaki, N. S. Bingham, A. Scholl, R. L. Stamps, and L. J. Heyderman, Nature Materials **16**, 1106 (2017).

[16] D. Y. Lee and P. Tierno, Physical Review Materials **2**, 112601(R) (2018).

[17] M. J. Harris, S. T. Bramwell, D. F. McMorrow, T. Zeiske and K. W. Godfrey, Physical Review Letter **79**, 2554 (1997).

[18] Y. Perrin, B. Canals, N. Rougemaille, Nature **540**, 410 (2016).

[19] A. Farhan, M. Saccone, C. F. Petersen, S. Dhuey, R. V. Chopdekar, Y.-L. Huang, N. Kent, Z. Chen, M. J. Alava, T. Lippert, A. Scholl, S. van Dijken, Science Advances **5**, eaav6380 (2019).

[20] M. Saccone, A. Scholl, S. Velten, S. Dhuey, K. Hofhuis, C. Wuth, Y.-L. Huang, Z. Chen, R. V. Chopdekar, and A. Farhan, Physical Review B **99**, 224403 (2019).

[21] I. Gilbert, G.-W. Chern, S. Zhang, L. O'Brien, B. Fore, C. Nisoli, and P. Schiffer, Nature Physics **10**, 670 (2014).

[22] A. Farhan, A. Scholl, C. F. Petersen, L. Anghinolfi, C. Wuth, S. Dhuey, R. V. Chopdekar, P. Mellado, M. J. Alava, and Sebastiaan van Dijken, Nature Communications **7**, 12635 (2016).

[23] G.-W. Chern, P. Mellado, Europhysics Letters **114**, 37004 (2016).

[24] J. Sklenar, Y. Lao, A. Albrecht, J. D. Watts, C. Nisoli, G.-W. Chern, and P. Schiffer, Nature Physics **15**, 191 (2019).

[25] J. Drisko, T. Marsh, and J. Cumings, Nature Communications **8**, 14009 (2017).

[26] B. Farmer, V. S. Bhat, A. Balk, E. Teipel, N. Smith, J. Unguris, D. J. Keavney, J. T. Hastings, and L. E. De Long, Physical Review B **93**, 134428 (2016).

[27] D. Shi, Z. Budrikis, A. Stein, S. A. Morley, P. D. Olmsted, G. Burnell, and C. H. Marrows, Nature Physics **14**, 309 (2018).

[28] V. Brajuskovic, A. Addi, C. Phatak, and A. K. Petford-Long, Physical Review B **98**, 094424 (2018).

[29] A. Farhan, C. F. Petersen, S. Dhuey, L. Anghinolfi, Q.-H. Qin, M. Saccone, S. Velten, C. Wuth, S. Gliga, P. Mellado, M. J. Alava, A. Scholl, and S. van Dijken, Nature Communications **8**, 995 (2017).

[30] C. F. Petersen, A. Farhan, S. Dhuey, Z. Chen, M. J. Alava, A. Scholl, and S. van Dijken, Applied Physics Letters **112**, 092403 (2018).

[31] Y.-L. Wang, Z.-L. Xiao, A. Snezhko, J. Xu, L. E. Ocola, R. Divan, J. E. Pearson, G. W. Crabtree, W.-K. Kwok, Science **352**, 962 (2016).

[32] V. M. Parakkat, K. Xie, and K. M. Krishnan, Physical Review B **99**, 054429 (2019).

[33] S. Gliga, A. Kákay, R. Hertel, and O. G. Heinonen, Physical Review Letters **110**, 117205 (2013).

[34] M. B. Jungfleisch, W. Zhang, E. Iacocca, J. Sklenar, J. Ding, W. Jiang, S. Zhang, J. E. Pearson, V. Novosad, J. B. Ketterson, O. Heinonen, and A. Hoffmann, Physical Review B **93**, 100401(R) (2016).

[35] V. S. Bhat, F. Heimbach, I. Stasinopoulos, and D. Grundler, Physical Review B **93**, 140401(R) (2016).

[36] C. Nisoli, R. Moessner, and P. Schiffer, Reviews of Modern Physics **85**, 1473 (2013).

[37] I. Rousochatzakis, A. M. Läuchli, and R. Moessner, Physical Review B **85**, 104415 (2012).

[38] A. M. Abakumov, D. Batuk, A. A. Tsirlin, C. Prescher, L. Dubrovinsky, D. V. Sheptyakov, W. Schnelle, J. Hadermann, and G. Van Tendeloo, Physical Review B **87**, 024423 (2013).

[39] M. Rojas, O. Rojas, and S. M. de Souza, Physical Review E **86**, 051116 (2012).

[40] A. A. Tsirlin, I. Rousochatzakis, D. Filimonov, D. Batuk, M. Frontzek, and A. M. Abakumov, Physical Review B **96**, 094420 (2017).

[41] A. Doran, M. Church, T. Miller, G. Morrison, A. T. Young, and A. Scholl, Journal of Electron Spectroscopy and Related Phenomena **185**, 340 (2012)., Journal of Electron Spectroscopy and Related Phenomena **185**, 340 (2012).

[42] J. Stöhr Y. Wu, B. D. Hermsmeier, M. G. Samant, G. R. Harp, S. Koranda, D. Dunham, and B. P. Tonner, Science **259**, 658 (1993).

[43] A. Farhan, A. Kleibert, P. M. Derlet, L. Anghinolfi, A. Balan, R. V. Chopdekar, M. Wyss, S. Gliga, F. Nolting, and L. J. Heyderman, Physical Review B **89**, 214405 (2014).

[44] A. Vansteenkiste, J. Leliaert, M. Dvornik, M. Helsen, F. Garcia-Sanchez, and B. Van Waeyenberge, AIP Advances **4**, 107133 (2014).

[45] C. Castelnovo, R. Moessner, S. L. Sondhi, Nature **451**, 42 (2008).

[46] G. Möller and R. Moessner, Physical Review B **80**, 140409(R) (2009).

[47] Y. Qi, T. Brintlinger, and J. Cumings, Physical Review B **77**, 094418 (2008).

[48] H. Stopfel, E. Östman, I.-A. Chioar, D. Greving, U. B. Arnalds, T. P. A. Hase, A. Stein, B. Hjörvarsson, and V. Kapaklis, Physical Review B **98**, 014435 (2018).

[49] G.W. Chern and O. Tchernyshyov. Philosophical Transactions of the Royal Society A: Mathematical, Physical and Engineering Sciences. **5718**, 370 (2012).

[50] I. Gilbert, Y. Lao, I. Carrasquillo, L. O'Brien, J. D. Watts, M. Manno, C. Leighton, A. Scholl, C. Nisoli, and P. Schiffer, Nature Physics **12**, 162 (2016).

[51] Y. Lao, F. Caravelli, M. Sheikh, J. Sklenar, D. Gardeazabal, J. D. Watts, A. M. Albrecht, A. Scholl, K. Dahmen, C. Nisoli, and P. Schiffer, Nature Physics **14**, 723 (2018).